

DROID-Splat

Combining end-to-end SLAM with 3D Gaussian Splatting

Christian Homeyer¹ Leon Begiristain¹ Christoph Schnörr¹
¹Image and Pattern Analysis Group, Heidelberg University, Germany

homeyer@math.uni-heidelberg.de, lbegirri7@alumnos.ub.edu, schnoerr@math.uni-heidelberg.de

Abstract

Recent progress in scene synthesis makes standalone SLAM systems purely based on optimizing hyperprimitives with a Rendering objective possible [24]. However, the tracking performance still lacks behind traditional [27] and end-to-end SLAM systems [41]. An optimal trade-off between robustness, speed and accuracy has not yet been reached, especially for monocular video. In this paper, we introduce a SLAM system based on an end-to-end Tracker and extend it with a Renderer based on recent 3D Gaussian Splatting techniques. Our framework **DroidSplat** achieves both SotA tracking and rendering results on common SLAM benchmarks. We implemented multiple building blocks of modern SLAM systems to run in parallel, allowing for fast inference on common consumer GPU's. Recent progress in monocular depth prediction and camera calibration allows our system to achieve strong results even on in-the-wild data without known camera intrinsics. Code will be available at <https://github.com/ChenHoy/DROID-Splat>.

1. Introduction

Simultaneous Localization and Mapping (SLAM) has been a longstanding problem in Computer Vision, fundamental to applications in robotics, autonomous driving and augmented reality. While traditional systems focus on reconstruction of accurate odometry and geometry from hand-crafted features, they usually result in sparse or semi-dense representations of the environment. End-to-end SLAM systems [21, 41, 42] improved robustness and accuracy by using learned features and a dense reconstruction objective, however they often lack the ability to optimize a photo-realistic scene. Recent progress in scene synthesis makes standalone SLAM systems purely based on optimizing hyperprimitives with a Rendering objective possible [24]. However, the tracking performance still lacks behind traditional [27] and end-to-end SLAM systems [41]. We aim to close this gap by combining the best of both worlds.

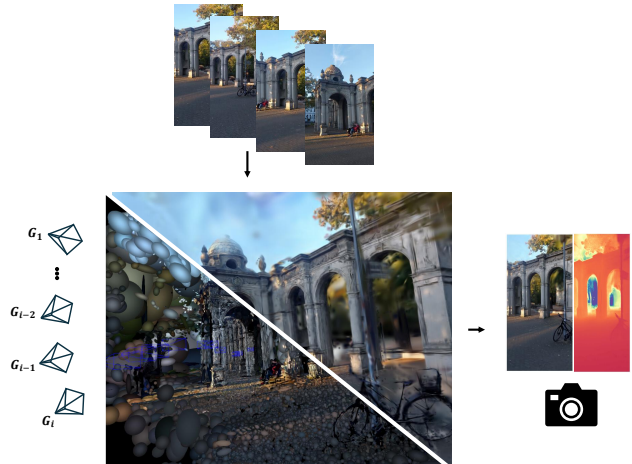


Figure 1. **DROID-Splat** allows to reconstruct a scene with known/unknown intrinsics. By combining an optical flow tracking objective and a fast, dense Renderer, we can achieve photo-realistic Reconstructions while optimizing accurate odometry.

In this paper, we introduce DROID-Splat: A SotA SLAM system based on dense, end-to-end optical flow and a dense Rendering objective using 3D Gaussian Splatting [18]. Our system offers the same flexibility as its parent system [41]: We support monocular and rgbd inference for different camera models (since we focus on single camera reconstruction, we neglect the stereo [41] or multi-view case [34]). By combining the best of both worlds, we achieve fast tracking inference on consumer GPU's and can quickly optimize a photo-realistic scene reconstruction. Our framework consists of a i) local frontend ii) global backend iii) loop closure detector iv) dense renderer. With this work we aim to systematically analyze the interplay of individual components and optimization objectives in more detail than previous work. A lot of recent SLAM frameworks have emerged, that focus on a single component. Our work aims to provide a comprehensive tool, which allows to easily reconstruct a scene from a video.

Monocular Video is notoriously difficult to reconstruct. For this reason we additionally allow integration of SotA

monocular depth prediction [2, 49, 51] priors similar to [56, 58] and concurrent work [33]. We show that with recent advances, it is possible to robustly handle in-the-wild data with unknown camera intrinsics. Using a depth prior and an additional camera calibration objective [10], we achieve strong reconstruction performance even on cellphone videos.

Our contributions are:

- We propose a dense SLAM system, which combines a dense end-to-end tracker with dense hyperprimitives.
- We combine common building blocks of modern SLAM systems in a fast parallel implementation. Our comprehensive ablations show which components really matter.
- We show SotA results on common SLAM benchmarks for both tracking and rendering in near real-time.
- Our framework is flexible with regards to input and works even on in-the-wild data with unknown intrinsics.

2. Related Work

Visual SLAM. Traditional SLAM systems can be categorized into *direct* or *indirect* [8] systems depending on their intermediate representation and objective function. Indirect approaches [27] make use of sparse feature descriptors for matching and then solve a geometric bundle adjustment problem. Direct approaches [7, 8] optimize a photometric error directly and operate on semi-dense pixel representations. However, direct approaches usually lead to more difficult optimization problems. Overcoming the limitation of both hand-crafted features and ill-behaved optimization, end-to-end SLAM systems [21, 41, 42] were proposed which allow a dense representation with well-behaved tracking. Long-term tracking requires a loop closure mechanism [21, 22, 27, 62]. Common frameworks memoize features of past frames to find similarities of new incoming frames to start a loop closure optimization, e.g. a Pose Graph Optimization [20]. On top of good odometry, common systems are concerned with a dense scene reconstruction. Traditional SLAM approaches either relied on voxel [3, 14, 28] or point [17, 35, 46] based map representations. These representations can allow a dense reconstruction, but are not photo-realistic.

Differentiable rendering. Neural Radiance Fields (NeRFs) [25] opened the gate to achieve photorealistic volume rendering, but training was initially slow. Using a multi-resolution hash encoding [26] enabled for the first time to use neural radiance fields in a SLAM context [30]. Recently, 3D Gaussian Splatting (3DGS) [18] has revolutionized the field. The real-time rendering and training quickly enabled numerous works to taylor a *direct* SLAM system based on the Rendering objective [16, 24, 48, 54]. However tracking remains to be behind the traditional counterparts. Combined hybrid systems [13, 33, 56] resolve this issue by combining the best of both worlds. Similar in fashion, we make use of a dense, robust end-to-end system [41] and combine it with

a renderer. We refer to [43] about more details on Rendering in SLAM.

Numerous works improve the original GS with new techniques [6, 12, 13, 19, 39, 44, 52, 53, 56, 60], some including better densification and pruning strategies [6, 52, 53] or better loss supervision [44]. We aim to leverage recent advances in diff. rendering in a SLAM context.

Concurrent Work. The most related work to us is [33], which similar to us, is based off DROID-SLAM [41] and 3DGS [18]. In the same manner, they make use of a previously proposed monocular prior integration [58]. However, we go beyond the monocular use case and analyze different input modes, renderer and additional camera calibration [10]. Moreover, we use a different loop closure mechanism and dive deeper into the interplay of tracker and renderer.

3. Our Approach

Since our goal is a photo-realistic dense scene reconstruction, we use a dense end-to-end tracker, which can provide reliable depth (or disparity) for each pixel. After filtering this map for only covisible points or areas of high confidence, we feed it into a rendering module, which optimizes Gaussian hyperprimitives for each pixel and densifies the scene based on a rendering objective. Due to the lightweight nature of Gaussian Splatting [18], we can run this rendering objective in real-time in parallel to our tracking system. An overview of our system can be seen in Figure 2. We systematically build up our system from common SLAM components. By unifying these techniques under one umbrella, we can reach state-of-the-art online photo-realistic reconstruction.

3.1. End-to-end Tracking

We base our tracker on online end-to-end system DROID-SLAM [41]. A frame-graph $(\mathcal{V}, \mathcal{E})$ is build from an incoming ordered stream of images $\{I_1, \dots, I_n\} \in \mathbb{R}^{N \times H \times W \times 3}$. This structure is in practice a keyframe buffer, storing our tracking state variables disparity $d_i \in \mathbb{R}^{H \times W}$ and camera pose $g_i \in SE(3)$. Dense optical flow is estimated by a recurrent neural network [40]. Given enough motion in the scene, a keyframe is inserted into the graph. An edge (i, j) signifies covisibility between the frames i and j . As this graph is dynamically build and maintained over the incoming stream, we perform differentiable Bundle Adjustment over the graph. Given the current state of poses and disparity, we can compute correspondences

$$p_{ij} = \Pi_c (G_{ij} \circ \Pi_c^{-1} (p_i, d_i)) \quad (1)$$

with the camera projection function Π . We use a pinhole camera model in all of our experiments, however similar to [10], we support multiple camera models in theory for this function. A correlation volume as in [40] can be indexed given p_{ij} , so we retrieve correlation features along an edge

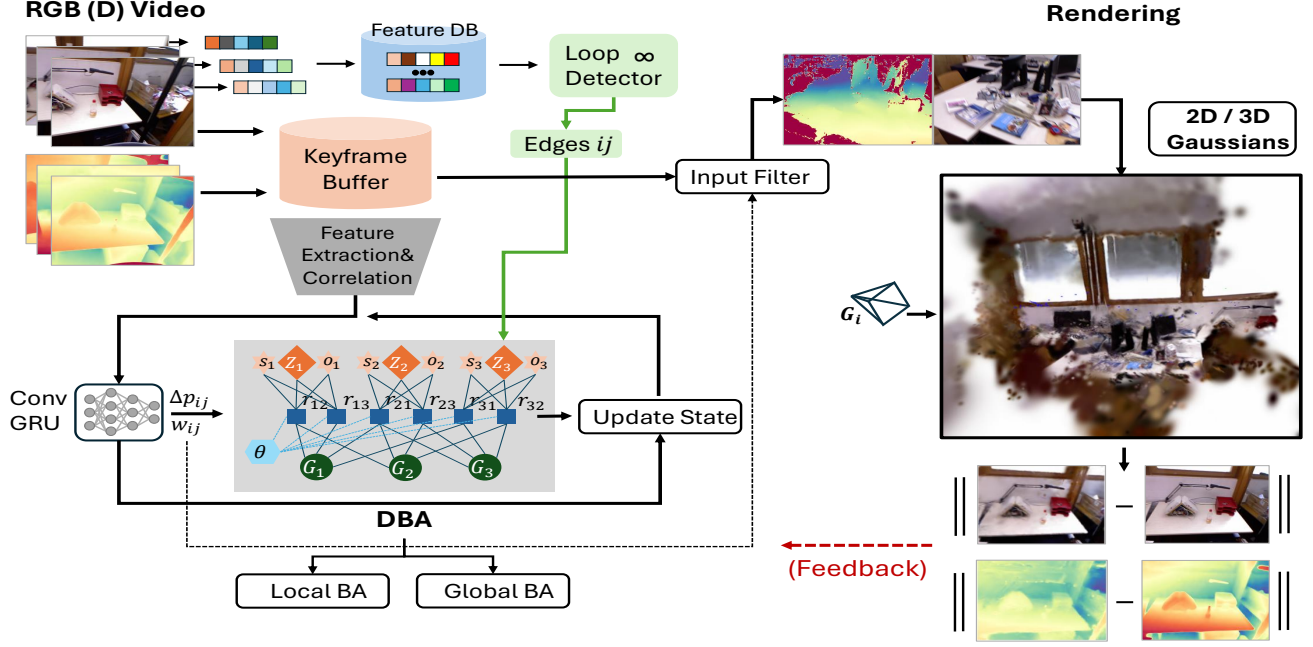


Figure 2. **DROID-Splat**. We make use of an end-to-end SLAM system with an optical flow based objective to perform tracking and reconstruct odometry and a dense initial map. The tracking objective is flexible, which allows us to optimize intrinsics or prior scale and shift as well if wanted. We make use of SotA Gaussian Splatting techniques to learn a photo-realistic reconstruction based on a Rendering objective. Since all components are differentiable and run in parallel, we can let parts interact flexibly.

(i, j) . The features, along with image context and a hidden state are input to a convolutional GRU to produce an update. The GRU produces i) the residual field $r_{ij} \in \mathbb{R}^{H \times W \times 2}$ and an associated confidence $w_{ij} \in \mathbb{R}^{H \times W \times 2}$. The residuals guide the current correspondences as $p_{ij}^* = r_{ij} + p_{ij}$. Together with the learned pose estimation confidence this powers a differentiable bundle adjustment optimization. Tracking is based on the reprojection based loss:

$$\mathbf{E}(\mathbf{G}', \mathbf{d}') = \sum_{(i,j) \in \mathcal{E}} \|\mathbf{p}_{ij}^* - \Pi_c(\mathbf{G}'_{ij} \circ \Pi_c^{-1}(\mathbf{p}_i, \mathbf{d}'_i))\|_{\Sigma_{ij}}^2$$

$$\Sigma_{ij} = \text{diag } \mathbf{w}_{ij} \quad . \quad (2)$$

This generic loss function can be used flexibly to not only supervise disparity d' and pose G' , but as shown in [10], we can also directly optimize the calibration of the camera with intrinsics θ :

$$\mathbf{E}(\mathbf{G}', \mathbf{d}', \theta) = \sum_{(i,j) \in \mathcal{E}} \|\mathbf{p}_{ij}^* - \Pi_c(\mathbf{G}'_{ij} \circ \mathbf{P}_i, \theta)\|_{\Sigma_{ij}}^2$$

$$\text{with } \mathbf{P}_i = \Pi_c^{-1}(\mathbf{p}_i, \mathbf{d}'_i, \theta) \quad (3)$$

Now [41] supports *RGBD-SLAM* by regularizing this with a prior term:

$$\mathbf{E}_{reg}(\mathbf{d}^*, \mathbf{d}') = \sum_{i \in \mathcal{V}} \|\mathbf{d}_i^* - \mathbf{d}'_i\|^2 \quad (4)$$

over a given input depth \mathbf{d}^* from an external sensor. Since we want to reconstruct any video, we make use of monocular

depth prediction priors [2, 49, 51]. Even though monocular depth prediction has made progress to predict accurate metric predictions [2, 51], there is considerable temporal fluctuations across the board of SotA monocular models. For this reason we optimize in what we call the *Pseudo-RGBD* mode, similar as [33, 56, 58]:

$$\mathbf{E}_{reg,m}(\mathbf{d}^*, \mathbf{d}', \mathbf{s}', \mathbf{o}') = \sum_{i \in \mathcal{V}} \|\mathbf{d}_i^* - (\mathbf{s}'_i \cdot \mathbf{d}'_i + \mathbf{o}'_i)\|^2 \quad (5)$$

After solving this bundle adjustment problem for a fixed number of iterations over the graph, we can update our state variables and continue until the next recurrence. In *P-RGBD* mode, we must be careful as an ambiguity between \mathbf{s} , \mathbf{o} and \mathbf{G} exists. For this reason like [58], we perform this in a block-coordinate descent manner, where we first fix scales and offsets and optimize poses. Afterwards we fix the pose graph and optimize structure, scales and offsets. We observe a similar ambiguity between intrinsics θ and the monocular variables. For this reason we operate in two stages on in-the-wild video inspired by [23]: 1. Fix the prior and use Eq.3 together with Eq. 4 to calibrate the camera. 2. Use the calibrated camera to run in *P-RGBD* mode with Eq. 5.

Modern SLAM systems [7, 27, 41] perform bundle adjustment normally on different parts of the map: i) A local frontend optimizes small-scale graphs for incoming keyframe windows ii) A global backend optimizes large-scale graphs with long-term connections over the whole map. While the original implementation [41] performs this on two separate

GPU’s, we run both Processes on a single GPU and perform these two optimizations synchronized in parallel. Monocular prior integration is performed on local frontend windows before the adjusted map is put into the backend. Camera intrinsics θ are treated as a global variable, that is optimized in the backend.

3.2. Loop Closure

We observe, that Visual Odometry accuracy and robustness depends not only on the optimization itself, but in particular on the graph structure of front- and backend. Accumulated drift can be compensated by running the Update operator on long-term connections of potential loop candidates. While [33, 59] detect candidates based on low apparent motion detected by the recurrent flow network [41], we had more success by using direct visual similarity. While systems as [21, 22, 27] rely on hand-crafted ORB features [31], we leverage recent end-to-end features from place recognition tasks [1]. For each incoming keyframe, we compute it’s visual features and insert them in a FAISS [4] database on the CPU. We then check for nearest neighbors in all past frames. Similar to [58], we only consider a frame pair (i, j) a loop candidate if i) The feature distance is small enough $d_{f,ij} < \tau_f$ ii) The camera orientation distance is small enough $d(\mathbf{R}_i, \mathbf{R}_j) < \tau_r$ and iii) the frames are far apart enough $|t_i - t_j| > \tau_t$. If a candidate pair is found, we augment the graph by adding a bi-directional edge to the backend. This Process runs in parallel on the CPU with a marginal additional cost.

3.3. Differentiable Rendering

Similar to previous works [13, 16, 24, 33] we utilize Gaussian hyperprimitives defined as a set of points $\mathbf{P} \in \mathbb{R}^3$ associated to our dense tracking map. Each Gaussian possesses a rotation $\mathbf{r} \in SO(3)$, scaling $\mathbf{s} \in \mathbb{R}^3$, density $\sigma \in \mathbb{R}^1$ and spherical harmonic coefficients $\mathbf{SH} \in \mathbb{R}^{16}$. We initialize the Gaussians similar to [24] by downsampling the map by a constant factor after triangulation. Gaussians are optimized via backpropagation on a dense Rendering loss. The rendering process [18] is defined as:

$$C(\mathbf{R}, \mathbf{t}) = \sum_{i \in \mathcal{N}} \mathbf{c}_i \alpha_i \prod_{j=1}^{i-1} (1 - \alpha_j), \quad (6)$$

where \mathbf{c} denotes the color converted from \mathbf{SH} and $\alpha_i = \sigma_i \cdot \mathcal{G}(\mathbf{R}, \mathbf{t}, \mathbf{P}_i, \mathbf{r}_i, \mathbf{s}_i)$. This allows us to render our map at given keyframe G_i to produce both an image I'_i and depth Z'_i . We follow [24] for median depth rendering. Gaussian Splatting [16, 18, 24] utilizes a mixed rendering loss

$$\begin{aligned} L_i &= \lambda_1 L_{rgb} + (1 - \lambda_1) L_{depth} \\ &= \lambda_1 [(1 - \lambda_2) \|I'_i - I_i^*\| + \lambda_2 (1 - SSIM(I'_i, I_i^*))] \\ &\quad + (1 - \lambda_1) \|Z'_i - Z_i^*\| \end{aligned} \quad (7)$$

which allows us to perform backpropagation by comparing with a reference I^*, Z^* . Each time we update our renderer, we optimize over a batch of cameras to improve our scene reconstruction. Since every component is differentiable, we can in theory optimize our keyframe poses with the rendering objective and feed them back into the tracker. We therefore want to research the questions: *Which objective is better suited for tracking? Can we improve our system further by finetuning with a dense rendering objective?*

Since we only improve the map by covering the whole 3D space with Gaussians, the original adaptive density control [18] strategy splits and clones Gaussians based on their size and gradient. This strategy was also used in any successful SLAM application [13, 16, 24, 33, 54]. It was recently observed, that this strategy is suboptimal and by guiding this process with a Monte Carlo Chain Markov (MCMC) model [19], we can improve performance. At the same time, this provides a preset upper limit of the total number of primitives. We compare these different strategies for our system and compare the 3D hyperprimitives themselves with the recently proposed 2D surfel Gaussians [12]. 2D Gaussian Splatting approximates surfaces by collapsing the primitives to flat surface disks, which result in more accurate geometry.

4. Experiments

We combine our components in a flexible way and ablate these choices in the following. During inference, we synchronize frontend, backend and renderer based on fixed frequencies, i.e. we run backend and renderer for every k_1, k_2 calls of the leading frontend process. The loop detector is constantly run in the background. If we detect a large tracking map update, we record the rel. transformations to reanchor our hyperprimitives. With mostly a stable map, we simply use a rigid body transformation $G \in SE(3)$ for this purpose. Gaussians are then typically in a position where they will quickly reconverge upon a new rendering optimization. For our monocular experiments with a prior, we use Metric3D [51] as it gave the most temporally consistent predictions without any scale optimization. We ablate this choice in the supplementary against multiple SotA models. We run our system on a NVIDIA RTX 4090. Similar to [24, 33] we do a refinement stage after running online tracking. We refine our map for 2k iterations and report the refined results for our final numbers. As benchmark metrics generally favor slower methods for this task, we report the detailed scaling of speed and performance in Fig. 4. We give more details on our system configuration, loss balancing and experiment settings in the supplementary.

Datasets. We evaluate our method on common SLAM benchmarks Replica [37] and TUM-RGBD [38]. We additionally showcase the ability of our system on self-recorded outdoor cellphone video.

Baselines. We compare ourselves to SotA pure Splatting

Components	ATE RMSE	ATE RMSE	ATE RMSE	ATE RMSE
	<i>KF</i> [cm]	<i>All</i> [cm]	<i>KF</i> [cm]	<i>All</i> [cm]
	TUM RGBD		Replica	
Frontend + Backend	4.88	5.22	2.51	2.47
+ scale opt.	1.92	1.80	0.273	0.273
+ Loop Detection	1.88	1.78	0.269	0.268
w Loop BA [59] Backend	3.91	3.61	0.53	0.52

Table 1. **Ablation Tracking.** We compare in *P-RGBD* mode, but observe that this is mostly consistent across input modes. Optimizing the scale of priors [51] is still important even when they are metric predictions. Using visual cues to find loop edges improves tracking.

Technique	PSNR \uparrow	LPIPS \downarrow	L1 \downarrow	PSNR \uparrow	LPIPS \downarrow	L1 \downarrow
	<i>KF</i>			<i>Non-KF</i>		
3DGS [18]	23.25	0.228	0.089	22.49	0.244	0.089
+ Covis. Pruning [24]	23.26	0.227	0.091	22.46	0.245	0.092
MCMC [19]	23.80	0.211	0.082	22.84	0.232	0.0843
+ Covis. Pruning [24]	23.78	0.214	0.82	22.81	0.234	0.0841
2DGS [12]	20.67	0.313	0.103	19.822	0.329	0.103
+ Covis. Pruning [24]	20.71	0.310	0.102	19.838	0.329	0.103

Table 2. **Ablation Rendering.** We compare a selection of recent advancements in rendering within our framework. Results are averaged over TUM RGBD [38], as this is one of the most challenging benchmarks. We test this in *P-RGBD* mode. See the supplementary for more techniques we have tried.

based SLAM frameworks [16, 24, 54] and hybrid systems [13, 33, 56] like ours. Finally, we also compare to systems based on volume rendering [59] or NeRF’s [29, 30].

Evaluation Metrics. For Rendering we report PSNR, SSIM [45] and LPIPS [57] on the rendered keyframe images against the groundtruth. For geometry, we compare the rendered depth L1 [cm] error to the groundtruth sensor as in [30]. In case of monocular depth, we compare the scale-aligned depth [2]. For tracking we compare the ATE RMSE [cm] [38] error on the estimated trajectory. Reported results are averaged over 5 runs for statistical significance.

Tracking Ablation. Table 1 shows the importance of individual tracking components in *P-RGBD* mode. These results are mostly consistent across input modes and datasets, see supplementary. We make the observation that the factor graph building process is of most importance.

Integrating monocular priors with the scale optimization is crucial. We did not have success with the Loop BA proposed in [59] in our Backend. Instead, we achieve the best results when adding visually similar loop candidates into our graph. We also want to highlight, that we achieve SotA results by simply utilizing a more conservative graph building strategy. See the supplementary for more details.

Renderer Ablation. Table 2 shows an ablation of recently proposed Gaussian Splatting techniques. For this

Method	fr1/ desk	fr2/ xyz	f3/ off	f1/ desk2	f1/ room	Avg.
Mono						
DPV-SLAM [21]	1.8	1.0	-	2.9	9.6	
GORIE-SLAM [56]	1.6	0.2	1.4	2.8	4.2	2.1
GO-SLAM [59]	1.6	0.6	1.5	2.8	5.2	2.3
MonoGS [24]	4.2	4.8	4.4	-	-	
MoD-SLAM [61]	1.5	0.7	1.1	-	-	
Photo-SLAM [13]	1.54	0.98	1.26	-	-	
Ours Mono	1.6	0.2	1.6	8.3	5.8	3.5
Ours P-RGBD	1.6	0.2	1.7	2.3	3.3	1.8
RGBD						
SplaTAM [16]	3.4	1.2	5.2	6.5	11.1	5.5
GS-SLAM [54]	1.5	1.6	1.7	-	-	
GO-SLAM [59]	1.5	0.6	1.3	2.8	5.2	2.3
Photo-SLAM [13]	2.6	0.35	1.0	-	-	
Ours RGBD	1.6	1.4	1.4	2.2	2.7	1.9

Table 3. **Tracking Performance TUM-RGBD [38]** (ATE RMSE \downarrow [cm]). Results are from respective papers. We achieve SotA tracking with our framework. Best results are highlighted as **first**, **second**, **third**.

ablation, we compare results without a refinement stage. We detail additional experiments in the supplementary. We want to highlight, that common comparisons should always factor in the total number of Gaussians used. We use 120k Gaussians on average on TUM-RGBD. Of course, using more primitives will improve photo-realism at the cost of memory and compute. We observe, that the covisibility pruning from [24] is not necessarily effective on indoor datasets. Naive map building can perform better, however at the price of a few thousand more Gaussians. By far the most effective improvement in our experiments is the MCMC guided densification strategy [19], which gives a consistent boost in rendering metrics compared to the naive gradient based densification strategy [18]. In order to make a fair comparison we match the total number of Gaussians to be equal with both strategies. 2D Gaussian Splatting turned out to be ineffective on very cluttered indoor scenes such as TUM-RGBD, either over-smoothing details or not building correct surfaces. We also observe, that optimizing geometry typically comes at the cost of worse rendering performance. We can control this trade-off by tuning λ_1 .

4.1. Comparison with the State-of-the-Art

We evaluate on synthetic and real-world scenes and compare with the State-of-the-Art. As can be seen in Table 3, we achieve competitive tracking performance on real world scenes. We want to highlight, that mostly *fr1/desk2* and *fr1/room* are challenging and therefore account biggest in the average. The performance of most frameworks seems similar on easier ones. We are also SotA on Replica across different modes in Table 4 and 5. It can be seen, that traditional and end-to-end tracking systems are still the best once perfect supervision is missing. However with perfect synthetic data, direct methods achieve strong results. Monocular methods, that utilize a depth prior [33, 56, 61] generally perform better on rendering and tracking due to the extra information. Our

Metric	NeRF-SLAM [30]	GO-SLAM [59]	NICER-SLAM [64]	MoD-SLAM [61]	Photo-SLAM [13]	Mono-GS [24]	GIORIE-SLAM [56]	Q-SLAM [29]	Splat-SLAM* [33]	Ours mono	Ours P-RGBD
PSNR \uparrow	41.40	22.13	25.41	27.31	33.30	31.22	31.04	32.49	36.45	39.47	39.66
SSIM \uparrow	-	0.73	0.83	0.85	0.93	0.91	0.97	0.89	0.95	1.0	1.0
LPIPS \downarrow	-	-	0.19	-	-	0.21	0.12	0.17	0.06	0.03	0.03
L1 \downarrow	4.49	4.39	-	3.23	-	27.24	-	2.76	2.41	3.33	3.34
ATE RMSE \downarrow	-	0.39	1.88	0.35	1.09	14.54	0.35	-	0.35	0.27	0.27

Table 4. **Avg. Rendering and Tracking Results on Replica [37]** for monocular methods. Results are from [43] and the respective papers.

Metric	Vox-Fusion [50]	NICE-SLAM [63]	Mono-GS [24]	Point-SLAM [32]	SplatAM [16]	Gaussian SLAM [54]	Photo-SLAM [13]	GO-SLAM [59]	Ours
PSNR \uparrow	24.42	26.16	38.94	35.17	34.11	42.08	34.96	-	39.66
SSIM \uparrow	0.81	0.83	0.97	0.98	0.97	1.0	0.94	-	1.0
LPIPS \downarrow	0.23	0.23	0.07	0.12	0.10	0.02	0.06	-	0.03
L1 \downarrow	-	-	-	-	-	-	-	3.38	0.55
ATE RMSE \downarrow	3.09	2.35	0.32*/0.58	0.53	0.36	0.31	0.60	0.34	0.29

Table 5. **Avg. Rendering and Tracking Results on Replica [37]** for RGB-D methods. Results are from the respective papers. *result comes from the slower single-process implementation.

method consistently ranks across the highest in rendering due to the dense representation both in tracker and renderer. Even though Photo-SLAM [13] utilizes a robust tracking system [27], the sparse hyperprimitive optimization does not

allow indistinguishable renders. Figure 3 shows rendered images and depth maps. We achieve highly detailed geometry on monocular video. Our monocular prior provides dense guidance even when laser sensors have holes. Table 6 show-

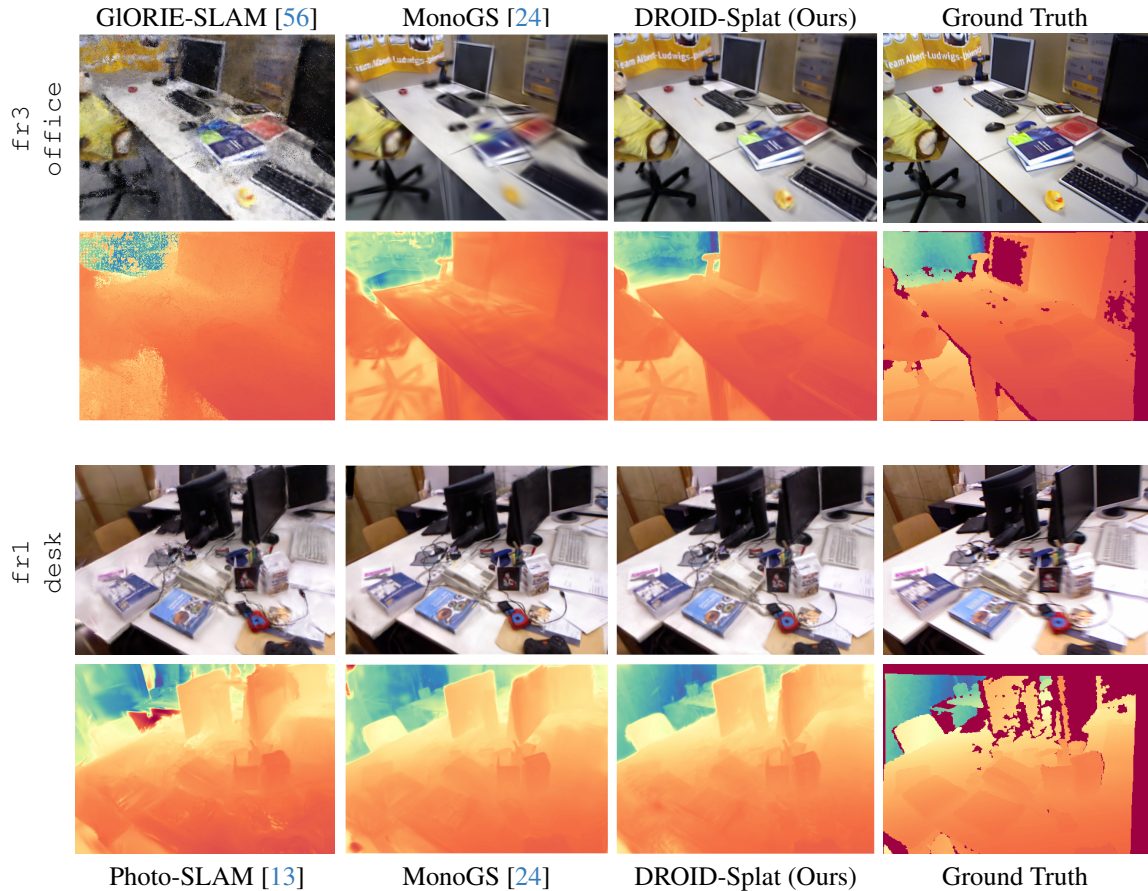


Figure 3. **Rendering Results on TUM-RGBD [38]**. We show views, that were not in the training set, i.e. our keyframe buffer. Top two rows show *monocular* methods, bottom shows *RGBD* (We show the results with prior for ours). We achieve a higher rendering and depth quality than [13, 24, 56] due to initializing with a dense tracking system and using dense hyperprimitives. Using a monocular prior can even improve upon a sparse laser sensor.

Method	Metric	f1/desk	f2/xyz	f3/off	f1/desk2	f1/room	Avg.
RGB-D							
SplaTaM [16]	PSNR↑	22.00	24.50	21.90	-	-	
	SSIM↑	0.86	0.95	0.88	-	-	
	LPIPS↓	0.23	0.10	0.20	-	-	
Gaussian-SLAM [54]	PSNR↑	24.01	25.02	26.13	23.15	22.98	24.26
	SSIM↑	0.92	0.92	0.94	0.91	0.89	0.92
	LPIPS↓	0.18	0.19	0.14	0.20	0.24	0.19
Photo-SLAM [13]	PSNR↑	20.87	22.09	22.74	-	-	
	SSIM↑	0.74	0.77	0.78	-	-	
	LPIPS↓	0.24	0.17	0.15	-	-	
Ours	PSNR↑	26.45	28.45	27.83	25.13	26.16	26.81
	SSIM↑	0.99	0.99	0.99	0.99	0.99	0.99
	LPIPS↓	0.12	0.07	0.10	0.15	0.14	0.12
Mono							
Photo-SLAM [13]	PSNR↑	20.97	21.07	19.59	-	-	
	SSIM↑	0.74	0.73	0.69	-	-	
	LPIPS↓	0.23	0.17	0.24	-	-	
MonoGS [24]	PSNR↑	19.67	16.17	20.63	19.16	18.41	18.81
	SSIM↑	0.73	0.72	0.77	0.66	0.64	0.70
	LPIPS↓	0.33	0.31	0.34	0.48	0.51	0.39
GIORIE-SLAM [56]	PSNR↑	20.26	25.62	21.21	19.09	18.78	20.99
	SSIM↑	0.79	0.72	0.72	0.92	0.73	0.77
	LPIPS↓	0.31	0.09	0.32	0.38	0.38	0.30
Splat-SLAM* [33]	PSNR↑	25.61	29.53	26.05	23.98	24.06	25.85
	SSIM↑	0.84	0.90	0.84	0.81	0.80	0.84
	LPIPS↓	0.18	0.08	0.20	0.23	0.24	0.19
Ours Mono	PSNR↑	26.72	29.35	27.92	24.58	25.64	26.84
	SSIM↑	0.99	0.99	0.99	0.99	0.99	0.99
	LPIPS↓	0.12	0.07	0.11	0.18	0.17	0.13
Ours P-RGBD	PSNR↑	26.42	28.08	27.84	25.21	25.11	26.53
	SSIM↑	0.99	0.99	0.99	0.99	0.99	0.99
	LPIPS↓	0.12	0.08	0.11	0.17	0.18	0.13

Table 6. **Rendering Performance on TUM-RGBD [38]**. Numbers are from respective papers. Our method performs competitively or better than related *RGB-D* methods with monocular input. We achieve SotA results across all modes.

cases the SotA on TUM-RGBD. We consistently achieve strong rendering metrics even on more challenging scenes like *fr1/room*. We provide a more detailed overlook in the supplementary with an evaluation protocol of non-training frames. We observe in our experiments, that the benefit of both monocular and sensor depth priors can be observed mainly in the $L1$ reconstruction metric and on non-training frames. The current evaluation protocol rewards overfitting the scene. We also want to highlight from Table 5, that the synthetic Replica [37] benchmark is saturated in *RGBD* mode. Predicted images and groundtruth are already indistinguishable at a PSNR of $\geq 39[dB]$. The same can be said about the predicted depths at $L1 \leq 0.6[cm]$. We did not achieve the same geometry quality on Replica as related work [29, 33, 61], however the comparison is not fair since the number of hyperprimitives and inference time was not published in addition. We believe, that with more refinement iterations, different input filter thresholds and loss hyperparameters, we could reach the same metrics. More details can be found in the supplementary.

Can our renderer improve tracking? We can feedback outputs of our rendering pipeline back into the tracking system and verify this idea on Replica. We can backpropagate gradients from rendering into our pose graph by finetuning

poses during the render updates. We then use the finetuned poses in our next tracking update during bundle adjustment.

Feedback	ATE RMSE KF [cm]	ATE RMSE All [cm]	PSNR↑	LPIPS↓	L1↓
Replica					
RGBD					
None	0.293	0.289	36.03	0.06	0.0076
Disparity	0.294	0.304	35.99	0.06	0.0076
Poses	0.277	0.273	36.26	0.06	0.0074
Both	0.28	0.289	36.19	0.06	0.0075
P-RGBD					
None	0.269	0.268	32.92	0.134	0.0374
Poses	0.356	0.348	32.95	0.134	0.0394
Both	0.34	0.349	32.9	0.135	0.04
TUM RGBD					
RGBD					
None	1.94	1.87	23.76	0.194	0.054
Disparity	1.99	1.92	23.65	0.199	0.055
Poses	1.98	1.89	23.72	0.197	0.056
Both	2.0	2.12	23.61	0.199	0.056

Table 7. **Feedback**. Since all components are differentiable, we can finetune the pose graph based on the rendering objective and feed this back into the tracking system. This requires a well initialized rendering system and good dense groundtruth supervision. We did not achieve stable results on more noisy monocular data. We compare the average result across the dataset over 5 runs without refinement.

We can also go one step further and use the rendering objective to densify the disparity state of the tracker. In

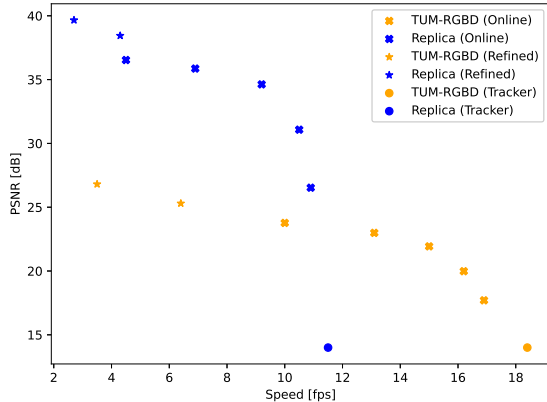


Figure 4. **Compute-Performance Trade-off.** We take the average across TUM RGBD [38] and Replica [37] in *RGBD* mode. We added the baseline Tracker at the bottom for perspective, this does not have a meaningful Metric attached to it.

practice we perform a check to make sure that the difference between rendered depth and tracker disparity is not too large in order to not confuse the update network. Table 7 shows different variations of this experiment in both *RGBD* mode with perfect groundtruth and in *P-RGBD* mode. We observe, that this actually works as long as perfect groundtruth is available. Results worsen when using a monocular prior or trying this idea on real data. We do not report monocular experiments on TUM-RGBD, because the stability of the tracker was severely affected.

Runtime analysis. The rendering performance heavily depends on how much compute is spend on optimizing the Gaussian primitives. We can give a scaling curve by adjusting the optimization iterations of the renderer or the frequency with which we use it. We also distinguish between online mode and offline refinement and give a baseline speed of our standalone tracker in Figure 4. We report results on the rendered keyframes. We want to note that in case of monocular depth priors, we are bottlenecked by the inference speed of the depth prediction network.

In-the-wild Reconstruction. For in-the-wild reconstruction, we tested both 3DGS [18] and 2DGS [12] on challenging outdoor scenes. We qualitatively analyzed both methods on self-recorded videos. The difference in rendering quality seems to prevail on unbounded outdoor scenes with no 360-degree camera trajectory. Due to the challenging lighting conditions and much more unreliable monocular depth priors, we accumulate many floater Gaussians. 2D Gaussian Splatting does not suffer as much from these, as it generates smooth surfaces. See Figure 5 for a visual comparison.

Failure Cases. Our method fails to handle challenging lighting changes and lens flares without additional modifications. In general, we perform much worse in sparser scenarios or when our priors are unreliable. We also observe, that although our tracking system is robust, it can

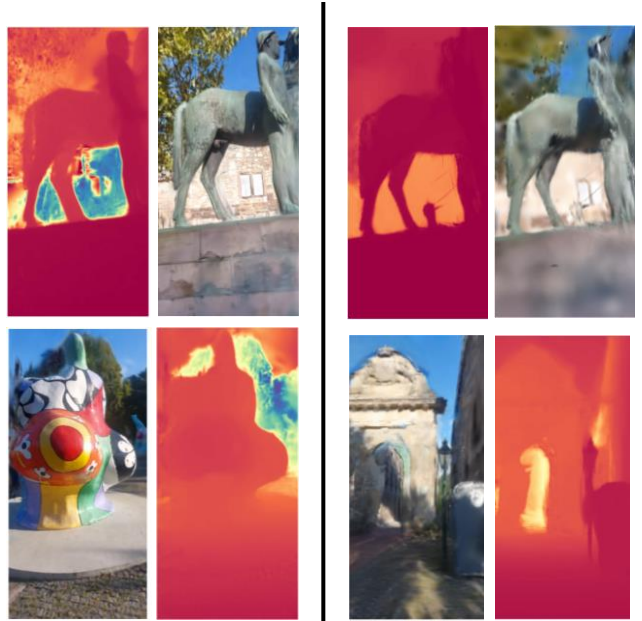


Figure 5. **Results on hand-captured cellphone videos.** In-the-wild outdoor scenes pose different challenges than benchmarks. *Left:* 3D Gaussian Splatting. *Right:* 2D Gaussian Splatting. While 2DGS is more resistant to floaters due to its surface optimization, it struggles with rendering quality. Both methods cannot deal well with strong lighting changes and reflections without extensions.

still drift on much more challenging scenes and trajectories. Since we optimize our hyperprimitives in batches, we are prone to catastrophic forgetting as other methods and need to reoptimize.

5. Conclusion

We combined a dense end-to-end SLAM system with a photo-realistic renderer. We systematically ablated common design choices and achieve SotA results with our framework on common benchmarks. The integration of recent monocular depth priors allowed to close the gap between monocular and RGBD SLAM both for odometry and rendering. Our experiments show, that photorealistic rendering and accurate geometry can be complementary objectives at this level, where improving rendering performance comes at a cost of worse geometry. At the same time, we did not see an improvement of our tracker based on the rendering objective for natural scenes. Our framework is flexible and can seamlessly reconstruct even in-the-wild video with unknown intrinsics.

Outlook. We hope that our Python framework enables rapid experimentation and further research in combining neural networks and SLAM. Recent foundation models [55] allow to infer 3D scenes from images directly without test-time optimization. The integration of such models poses an exciting avenue for future research. Extending the system to larger complex scenes would be another interesting direction.

ACKNOWLEDGMENT. We would like to say a special thank you to Andrei Prioteasa for helping setup the experiments and our colleagues at the Institute of Applied Mathematics, Heidelberg for fruitful discussions.

References

- [1] Gabriele Berton, Gabriele Trivigno, Barbara Caputo, and Carlo Masone. Eigenplaces: Training viewpoint robust models for visual place recognition. In *Proceedings of the IEEE/CVF International Conference on Computer Vision*, pages 11080–11090, 2023. [2](#), [3](#), [5](#), [17](#), [18](#)
- [2] Shariq Farooq Bhat, Reiner Birkl, Diana Wofk, Peter Wonka, and Matthias Müller. Zoedepth: Zero-shot transfer by combining relative and metric depth. *arXiv preprint arXiv:2302.12288*, 2023. [2](#), [3](#), [5](#), [17](#), [18](#)
- [3] Angela Dai, Matthias Nießner, Michael Zollhöfer, Shahram Izadi, and Christian Theobalt. Bundlefusion: Real-time globally consistent 3d reconstruction using on-the-fly surface reintegration. *ACM Transactions on Graphics (ToG)*, 36(4):1, 2017. [2](#)
- [4] Matthijs Douze, Alexandr Guzhva, Chengqi Deng, Jeff Johnson, Gergely Szilvassy, Pierre-Emmanuel Mazaré, Maria Lomeli, Lucas Hosseini, and Hervé Jégou. The faiss library. *arXiv preprint arXiv:2401.08281*, 2024. [4](#)
- [5] Xiaobiao Du, Yida Wang, and Xin Yu. Mvgs: Multi-view-regulated gaussian splatting for novel view synthesis, 2024. [19](#)
- [6] Xiaobiao Du, Yida Wang, and Xin Yu. Mvgs: Multi-view-regulated gaussian splatting for novel view synthesis, 2024. [2](#)
- [7] Jakob Engel, Thomas Schöps, and Daniel Cremers. Lsd-slam: Large-scale direct monocular slam. In *European conference on computer vision*, pages 834–849. Springer, 2014. [2](#), [3](#)
- [8] Jakob Engel, Vladlen Koltun, and Daniel Cremers. Direct sparse odometry. *IEEE transactions on pattern analysis and machine intelligence*, 40(3):611–625, 2017. [2](#)
- [9] Andreas Geiger, Philip Lenz, and Raquel Urtasun. Are we ready for autonomous driving? the kitti vision benchmark suite. In *2012 IEEE conference on computer vision and pattern recognition*, pages 3354–3361. IEEE, 2012. [17](#)
- [10] Annika Hagemann, Moritz Knorr, and Christoph Stiller. Deep geometry-aware camera self-calibration from video. In *Proceedings of the IEEE/CVF International Conference on Computer Vision*, pages 3438–3448, 2023. [2](#), [3](#), [18](#)
- [11] Jing He, Haodong Li, Wei Yin, Yixun Liang, Leheng Li, Kaiqiang Zhou, Hongbo Zhang, Bingbing Liu, and Ying-Cong Chen. Lotus: Diffusion-based visual foundation model for high-quality dense prediction. *arXiv preprint arXiv:2409.18124*, 2024. [17](#), [18](#)
- [12] Binbin Huang, Zehao Yu, Anpei Chen, Andreas Geiger, and Shenghua Gao. 2d gaussian splatting for geometrically accurate radiance fields. In *ACM SIGGRAPH 2024 Conference Papers*, pages 1–11, 2024. [2](#), [4](#), [5](#), [8](#), [12](#), [16](#)
- [13] Huajian Huang, Longwei Li, Hui Cheng, and Sai-Kit Yeung. Photo-slam: Real-time simultaneous localization and photo-realistic mapping for monocular stereo and rgb-d cameras. In *Proceedings of the IEEE/CVF Conference on Computer Vision and Pattern Recognition*, pages 21584–21593, 2024. [2](#), [4](#), [5](#), [6](#), [7](#), [14](#)
- [14] Olaf Kähler, Victor Adrian Prisacariu, Carl Yuheng Ren, Xin Sun, Philip H. S. Torr, and David William Murray. Very high frame rate volumetric integration of depth images on mobile devices. *IEEE Trans. Vis. Comput. Graph.*, 21(11):1241–1250, 2015. [2](#)
- [15] Bingxin Ke, Anton Obukhov, Shengyu Huang, Nando Metzger, Rodrigo Caye Daudt, and Konrad Schindler. Repurposing diffusion-based image generators for monocular depth estimation. In *Proceedings of the IEEE/CVF Conference on Computer Vision and Pattern Recognition*, pages 9492–9502, 2024. [18](#)
- [16] Nikhil Keetha, Jay Karhade, Krishna Murthy Jatavallabhula, Gengshan Yang, Sebastian Scherer, Deva Ramanan, and Jonathon Luiten. Splatam: Splat track & map 3d gaussians for dense rgb-d slam. In *Proceedings of the IEEE/CVF Conference on Computer Vision and Pattern Recognition*, pages 21357–21366, 2024. [2](#), [4](#), [5](#), [6](#), [7](#)
- [17] Maik Keller, Damien Lefloch, Martin Lambers, Shahram Izadi, Tim Weyrich, and Andreas Kolb. Real-time 3d reconstruction in dynamic scenes using point-based fusion. In *2013 International Conference on 3D Vision-3DV 2013*, pages 1–8. IEEE, 2013. [2](#)
- [18] Bernhard Kerbl, Georgios Kopanas, Thomas Leimkühler, and George Drettakis. 3d gaussian splatting for real-time radiance field rendering. *ACM Trans. Graph.*, 42(4):139–1, 2023. [1](#), [2](#), [4](#), [5](#), [8](#), [12](#), [13](#), [16](#), [18](#), [19](#)
- [19] Shakiba Kheradmand, Daniel Rebain, Gopal Sharma, Weiwei Sun, Jeff Tseng, Hossam Isack, Abhishek Kar, Andrea Tagliasacchi, and Kwang Moo Yi. 3d gaussian splatting as markov chain monte carlo, 2024. [2](#), [4](#), [5](#), [12](#), [13](#), [16](#)
- [20] Rainer Kümmerle, Giorgio Grisetti, Hauke Strasdat, Kurt Konolige, and Wolfram Burgard. g 2 o: A general framework for graph optimization. In *2011 IEEE international conference on robotics and automation*, pages 3607–3613. IEEE, 2011. [2](#)
- [21] Lahav Lipson, Zachary Teed, and Jia Deng. Deep patch visual slam. *arXiv preprint arXiv:2408.01654*, 2024. [1](#), [2](#), [4](#), [5](#)
- [22] Lorenzo Liso, Erik Sandström, Vladimir Yugay, Luc Van Gool, and Martin R Oswald. Loopy-slam: Dense neural slam with loop closures. In *Proceedings of the IEEE/CVF Conference on Computer Vision and Pattern Recognition*, pages 20363–20373, 2024. [2](#), [4](#)
- [23] Yu-Lun Liu, Chen Gao, Andreas Meuleman, Hung-Yu Tseng, Ayush Saraf, Changil Kim, Yung-Yu Chuang, Johannes Kopf, and Jia-Bin Huang. Robust dynamic radiance fields. In *Proceedings of the IEEE/CVF Conference on Computer Vision and Pattern Recognition*, pages 13–23, 2023. [3](#)
- [24] Hidenobu Matsuki, Riku Murai, Paul HJ Kelly, and Andrew J Davison. Gaussian splatting slam. In *Proceedings of the IEEE/CVF Conference on Computer Vision and Pattern Recognition*, pages 18039–18048, 2024. [1](#), [2](#), [4](#), [5](#), [6](#), [7](#), [12](#), [14](#)
- [25] Ben Mildenhall, Pratul P. Srinivasan, Matthew Tancik, Jonathan T. Barron, Ravi Ramamoorthi, and Ren Ng. Nerf:

- Representing scenes as neural radiance fields for view synthesis, 2020. [2](#)
- [26] Thomas Müller, Alex Evans, Christoph Schied, and Alexander Keller. Instant neural graphics primitives with a multi-resolution hash encoding. *ACM transactions on graphics (TOG)*, 41(4):1–15, 2022. [2](#)
- [27] Raul Mur-Artal, Jose Maria Martinez Montiel, and Juan D Tardos. Orb-slam: a versatile and accurate monocular slam system. *IEEE transactions on robotics*, 31(5):1147–1163, 2015. [1](#), [2](#), [3](#), [4](#), [6](#)
- [28] Matthias Nießner, Michael Zollhöfer, Shahram Izadi, and Marc Stamminger. Real-time 3d reconstruction at scale using voxel hashing. *ACM Transactions on Graphics (TOG)*, 32, 2013. [2](#)
- [29] Chensheng Peng, Chenfeng Xu, Yue Wang, Mingyu Ding, Heng Yang, Masayoshi Tomizuka, Kurt Keutzer, Marco Pavone, and Wei Zhan. Q-slam: Quadric representations for monocular slam. *arXiv preprint arXiv:2403.08125*, 2024. [5](#), [6](#), [7](#)
- [30] Antoni Rosinol, John J Leonard, and Luca Carlone. Nerf-slam: Real-time dense monocular slam with neural radiance fields. In *2023 IEEE/RSJ International Conference on Intelligent Robots and Systems (IROS)*, pages 3437–3444. IEEE, 2023. [2](#), [5](#), [6](#)
- [31] Ethan Rublee, Vincent Rabaud, Kurt Konolige, and Gary Bradski. Orb: An efficient alternative to sift or surf. In *2011 International conference on computer vision*, pages 2564–2571. Ieee, 2011. [4](#)
- [32] Erik Sandström, Yue Li, Luc Van Gool, and Martin R Oswald. Point-slam: Dense neural point cloud-based slam. In *Proceedings of the IEEE/CVF International Conference on Computer Vision*, pages 18433–18444, 2023. [6](#)
- [33] Erik Sandström, Keisuke Tateno, Michael Oechsle, Michael Niemeyer, Luc Van Gool, Martin R Oswald, and Federico Tombari. Splat-slam: Globally optimized rgb-only slam with 3d gaussians. *arXiv preprint arXiv:2405.16544*, 2024. [2](#), [3](#), [4](#), [5](#), [6](#), [7](#), [13](#)
- [34] Aron Schmied, Tobias Fischer, Martin Danelljan, Marc Pollefeys, and Fisher Yu. R3d3: Dense 3d reconstruction of dynamic scenes from multiple cameras. In *Proceedings of the IEEE/CVF International Conference on Computer Vision*, pages 3216–3226, 2023. [1](#)
- [35] Thomas Schops, Torsten Sattler, and Marc Pollefeys. Bad slam: Bundle adjusted direct rgb-d slam. In *Proceedings of the IEEE/CVF Conference on Computer Vision and Pattern Recognition*, pages 134–144, 2019. [2](#)
- [36] Nathan Silberman, Derek Hoiem, Pushmeet Kohli, and Rob Fergus. Indoor segmentation and support inference from rgb-d images. In *Computer Vision–ECCV 2012: 12th European Conference on Computer Vision, Florence, Italy, October 7–13, 2012, Proceedings, Part V 12*, pages 746–760. Springer, 2012. [17](#)
- [37] Julian Straub, Thomas Whelan, Lingni Ma, Yufan Chen, Erik Wijmans, Simon Green, Jakob J Engel, Raul Mur-Artal, Carl Ren, Shobhit Verma, et al. The replica dataset: A digital replica of indoor spaces. *arXiv preprint arXiv:1906.05797*, 2019. [4](#), [6](#), [7](#), [8](#), [12](#), [13](#), [15](#), [18](#)
- [38] Jürgen Sturm, Nikolas Engelhard, Felix Endres, Wolfram Burgard, and Daniel Cremers. A benchmark for the evaluation of rgb-d slam systems. In *2012 IEEE/RSJ international conference on intelligent robots and systems*, pages 573–580. IEEE, 2012. [4](#), [5](#), [6](#), [7](#), [8](#), [12](#), [13](#), [14](#), [16](#), [18](#)
- [39] Shuo Sun, Malcolm Mielle, Achim J Lilienthal, and Martin Magnusson. High-fidelity slam using gaussian splatting with rendering-guided densification and regularized optimization. *arXiv preprint arXiv:2403.12535*, 2024. [2](#), [19](#)
- [40] Zachary Teed and Jia Deng. Raft: Recurrent all-pairs field transforms for optical flow. In *Computer Vision–ECCV 2020: 16th European Conference, Glasgow, UK, August 23–28, 2020, Proceedings, Part II 16*, pages 402–419. Springer, 2020. [2](#)
- [41] Zachary Teed and Jia Deng. Droid-slam: Deep visual slam for monocular, stereo, and rgb-d cameras. *Advances in neural information processing systems*, 34:16558–16569, 2021. [1](#), [2](#), [3](#), [4](#), [12](#), [19](#)
- [42] Zachary Teed, Lahav Lipson, and Jia Deng. Deep patch visual odometry. *Advances in Neural Information Processing Systems*, 36, 2024. [1](#), [2](#)
- [43] Fabio Tosi, Youmin Zhang, Ziren Gong, Erik Sandström, Stefano Mattocchia, Martin R Oswald, and Matteo Poggi. How nerfs and 3d gaussian splatting are reshaping slam: a survey. *arXiv preprint arXiv:2402.13255*, 4, 2024. [2](#), [6](#)
- [44] Matias Turkulainen, Xuqian Ren, Iaroslav Melekhov, Otto Seiskari, Esa Rahtu, and Juho Kannala. Dn-splatter: Depth and normal priors for gaussian splatting and meshing, 2024. [2](#)
- [45] Zhou Wang, Alan C Bovik, Hamid R Sheikh, and Eero P Simoncelli. Image quality assessment: from error visibility to structural similarity. *IEEE transactions on image processing*, 13(4):600–612, 2004. [5](#), [12](#)
- [46] Thomas Whelan, Stefan Leutenegger, Renato F Salas-Moreno, Ben Glocker, and Andrew J Davison. Elasticfusion: Dense slam without a pose graph. In *Robotics: science and systems*, page 3. Rome, Italy, 2015. [2](#)
- [47] Haolin Xiong, Sairisheek Muttukuru, Rishi Upadhyay, Pradyumna Chari, and Achuta Kadambi. SparseSegs: Real-time 360° sparse view synthesis using gaussian splatting. *Arxiv*, 2023. [19](#)
- [48] Chi Yan, Delin Qu, Dan Xu, Bin Zhao, Zhigang Wang, Dong Wang, and Xuelong Li. Gs-slam: Dense visual slam with 3d gaussian splatting. In *Proceedings of the IEEE/CVF Conference on Computer Vision and Pattern Recognition*, pages 19595–19604, 2024. [2](#)
- [49] Lihe Yang, Bingyi Kang, Zilong Huang, Xiaogang Xu, Jiashi Feng, and Hengshuang Zhao. Depth anything: Unleashing the power of large-scale unlabeled data. In *Proceedings of the IEEE/CVF Conference on Computer Vision and Pattern Recognition*, pages 10371–10381, 2024. [2](#), [3](#), [17](#), [18](#)
- [50] Xingrui Yang, Hai Li, Hongjia Zhai, Yuhang Ming, Yuqian Liu, and Guofeng Zhang. Vox-fusion: Dense tracking and mapping with voxel-based neural implicit representation. In *2022 IEEE International Symposium on Mixed and Augmented Reality (ISMAR)*, pages 499–507. IEEE, 2022. [6](#)
- [51] Wei Yin, Chi Zhang, Hao Chen, Zhipeng Cai, Gang Yu, Kaixuan Wang, Xiaozhi Chen, and Chunhua Shen. Metric3d:

- Towards zero-shot metric 3d prediction from a single image. In *Proceedings of the IEEE/CVF International Conference on Computer Vision*, pages 9043–9053, 2023. 2, 3, 4, 5, 13, 16, 17, 18
- [52] Zehao Yu, Anpei Chen, Binbin Huang, Torsten Sattler, and Andreas Geiger. Mip-splatting: Alias-free 3d gaussian splatting. In *Proceedings of the IEEE/CVF Conference on Computer Vision and Pattern Recognition*, pages 19447–19456, 2024. 2
- [53] Zehao Yu, Torsten Sattler, and Andreas Geiger. Gaussian opacity fields: Efficient adaptive surface reconstruction in unbounded scenes, 2024. 2
- [54] Vladimir Yugay, Yue Li, Theo Gevers, and Martin R Oswald. Gaussian-slam: Photo-realistic dense slam with gaussian splatting. *arXiv preprint arXiv:2312.10070*, 2023. 2, 4, 5, 6, 7
- [55] Chubin Zhang, Hongliang Song, Yi Wei, Yu Chen, Jiwen Lu, and Yansong Tang. Geolrm: Geometry-aware large reconstruction model for high-quality 3d gaussian generation. *arXiv preprint arXiv:2406.15333*, 2024. 8
- [56] Ganlin Zhang, Erik Sandström, Youmin Zhang, Manthan Patel, Luc Van Gool, and Martin R Oswald. Glorie-slam: Globally optimized rgb-only implicit encoding point cloud slam. *arXiv preprint arXiv:2403.19549*, 2024. 2, 3, 5, 6, 7, 14
- [57] Richard Zhang, Phillip Isola, Alexei A Efros, Eli Shechtman, and Oliver Wang. The unreasonable effectiveness of deep features as a perceptual metric. In *Proceedings of the IEEE conference on computer vision and pattern recognition*, pages 586–595, 2018. 5
- [58] Wei Zhang, Tiecheng Sun, Sen Wang, Qing Cheng, and Norbert Haala. Hi-slam: Monocular real-time dense mapping with hybrid implicit fields. *IEEE Robotics and Automation Letters*, 2023. 2, 3, 4
- [59] Youmin Zhang, Fabio Tosi, Stefano Mattoccia, and Matteo Poggi. Go-slam: Global optimization for consistent 3d instant reconstruction. In *Proceedings of the IEEE/CVF International Conference on Computer Vision*, pages 3727–3737, 2023. 4, 5, 6
- [60] Zheng Zhang, Wenbo Hu, Yixing Lao, Tong He, and Hengshuang Zhao. Pixel-gs: Density control with pixel-aware gradient for 3d gaussian splatting. *arXiv preprint arXiv:2403.15530*, 2024. 2
- [61] Heng Zhou, Zhetao Guo, Shuhong Liu, Lechen Zhang, Qihao Wang, Yuxiang Ren, and Mingrui Li. Mod-slam: Monocular dense mapping for unbounded 3d scene reconstruction. *arXiv preprint arXiv:2402.03762*, 2024. 5, 6, 7
- [62] Liyuan Zhu, Yue Li, Erik Sandström, Konrad Schindler, and Iro Armeni. Loopsplat: Loop closure by registering 3d gaussian splats. *arXiv preprint arXiv:2408.10154*, 2024. 2
- [63] Zihan Zhu, Songyou Peng, Viktor Larsson, Weiwei Xu, Hujun Bao, Zhaopeng Cui, Martin R Oswald, and Marc Pollefeys. Nice-slam: Neural implicit scalable encoding for slam. In *Proceedings of the IEEE/CVF conference on computer vision and pattern recognition*, pages 12786–12796, 2022. 6
- [64] Zihan Zhu, Songyou Peng, Viktor Larsson, Zhaopeng Cui, Martin R Oswald, Andreas Geiger, and Marc Pollefeys. Nicer-slam: Neural implicit scene encoding for rgb slam. In *2024 International Conference on 3D Vision (3DV)*, pages 42–52. IEEE, 2024. 6

Supplementary Material

In this supplementary material, we provide more details on our approach, experiment settings and further experimental results. We encourage readers to take a look at our open-sourced implementation upon publication for more detailed configuration. All experiments are performed on a desktop computer with an *AMD Ryzen Threadripper PRO 5955WX* CPU and *NVIDIA RTX4090* GPU.

1. Inference settings and hyperparameters

We run our system at resolution 320×432 on TUM-RGBD [38] and 360×640 on Replica [37].

1.1. Tracking

Tracking is configured by the *frontend* and *backend* parameters for graph building, optimization and our loop detector. Since the configuration system is quite complex, we will only brush across the critical parameter settings. We will release full configurations upon publication.

Frontend. We use a motion threshold of 3.0 for adding new keyframes. During scale optimization we use the objective

$$E = E + \alpha E_{reg} \quad (8)$$

with $\alpha = 0.001$. We found it important to keep keyframes longer in the frontend bundle adjustment window. This can be controlled with the *max age* variable in [41]. We increase this value from 25 to 30. We use a weight $\beta = 0.5$ on TUM-RGBD [38] and $\beta = 0.7$ on Replica [37] for measuring frame distance, see [41].

Backend. We run the backend every 8 frontend passes in our experiments. We build our global graph more conservatively by using a window of max. 150 frames, using up to 1500 edges.

Loop Detector. We compute visual features by using the EigenPlaces [1] ResNet50 network. We found qualitatively, that a feature threshold $\tau_f = 0.5$ works well in practice. We make the assumption that loop candidates are at least $\tau_t = 10$ frames apart. For our orientation threshold, we set $\tau_r = 15^\circ$. This assumes that during a loop closure we have a very similar orientation, but due to drift a very distinct translation.

1.2. Rendering

We run our mapper every 20 frontend calls and optimize for 100 iterations at a small delay of 5 frames. We found that in practice, this can be arbitrarily tuned, i.e. we could also run more frequent with less training iterations. We anneal a 3D positional learning rate between $[1e - 4, 1e - 6]$ during our

optimization, the other parameters are similar to [24]. During each iteration, we optimize newly added frames and add the 10 last frames and 20 random past frames similar to [24]. Since we run a test-time optimization, we are also prone to catastrophic forgetting. Using enough random frames ensures that this does not happen. Our system is not yet designed to handle large-scale scenes or unbounded scenes, where smarter strategies may be needed.

After filtering the tracking map with a covisibility check [41], we downsample the point cloud with factor 64 on Replica [37] and 16 on TUM-RGBD [38]. We use the same thresholds for densification across datasets. We made the experience that balancing these parameters can result in similar results as long as the total number of Gaussians is similar. We weight $L1$ -error and $SSIM$ [45] in our appearance loss with $\lambda_2 = 0.2$. We balance depth and appearance supervision with $\lambda_1 = 0.9$ on TUM-RGBD [38] and 0.8 on Replica [37]. Balancing these two terms, can shift metrics slightly in favor of either appearance or geometry. Similar to [24] we encourage isotropic Gaussians with their scale regularization term. Our officially reported metrics are for dense depth supervision when a prior exists. For monocular video, we use the filtered tracking map as depth guidance.

Monte Carlo Markov Chain Gaussian Splatting. MCMC Gaussian Splatting [19] has additional hyperparameters for the noise level and the max. number of Gaussians in a scene. This poses an upper limit beyond which cannot be densified. We use $lr_{noise} = 1e4$ and use a slightly lower number of Gaussians from the runs with vanilla 3D Gaussian Splatting [18].

2D Gaussian Splatting 2D Gaussian Splatting has a slightly different objective function [12]. On top of the default rendering objective, we also have a normal consistency L_{normal} and depth distortion loss L_{dist} . We also found, that this representation has a different learning dynamic than 3D Gaussians. We therefore tuned the weighting to the best of our ability (without extensive parameter sweeps).

1.3. Feedback

In our feedback experiment, we perform backpropagation on the local pose graph of our rendering batch as is done in [24]. We used vanilla 3D Gaussian Splatting with the adaptive density control densification strategy [18]. As a sanity check, we only feedback the poses and/or disparity of rendered frames that have a decently similar disparity to the tracking map. The reason for this lies in the fact that our renderer has a small delay behind the leading tracker. If the rendering map is yet not covering enough pixels for some reason, we could potentially feedback a much sparser frame than we initially used during tracking. This could potentially disturb the update network [41]. We therefore

Technique	#Gaussians	PSNR \uparrow	KF		Non-KF		
			LPIPS \downarrow	L1 \downarrow	PSNR \uparrow	LPIPS \downarrow	L1 \downarrow
<i>TUM-RGBD</i>							
Monocular	118 889	26.84	0.129	16.67	24.62	0.156	17.37
P-RGBD	119 100	26.53	0.131	8.50	24.81	0.155	8.38
RGBD	123 232	26.81	0.110	4.26	24.89	0.144	4.63
<i>Replica</i>							
Monocular	246 637	39.47	0.031	3.33	38.42	0.032	3.47
P-RGBD	248 175	38.33	0.032	3.72	38.34	0.033	3.83
RGBD	235 825	39.66	0.028	0.55	38.87	0.029	0.61

Table 8. **Full Rendering results.** We report our overall best results with MCMC densification [19] averaged over 5 runs on TUM-RGBD [38] and Replica [37] with refinement.

Supervision	#Gaussians	PSNR \uparrow	KF		Non-KF		
			LPIPS \downarrow	L1 \downarrow	PSNR \uparrow	LPIPS \downarrow	L1 \downarrow
<i>TUM-RGBD</i>							
dense	88 280	25.98	0.140	8.2	24.48	0.161	8.2
sparse	100 156	24.37	0.129	15.6	24.37	0.155	16.7
<i>Replica</i>							
dense	264 343	38.79	0.0361	3.55	37.84	0.0371	3.64
sparse	275 997	38.95	0.0347	2.96	37.82	0.0361	3.11

Table 9. **Sparse vs. dense supervision of vanilla 3D Gaussian Splatting [18] with monocular prior.** Geometry reconstruction depends heavily on the degree and quality of supervision. TUM-RGBD [38] does not have enough redundancy in frames for the filtered map to cover the scene. Replica [37] on the other hand will produce enough reliable covisible 3D points, such that the filtered tracking map provides strong supervision for each Gaussian. For this reason, we can achieve better results when using the sparser, filtered map on Replica. This closes the gap to related work [33]. We believe that with different priors and hyperparameters, we would achieve the same $L1$ error.

check that the abs. rel. error between rendered disparity and tracking disparity is ≤ 0.2 . If at least 50% of pixels satisfy this condition, then the frame is considered good.

2. Extended Evaluation

In this section, we want to provide more insights into how our system performs quantitatively and show more qualitative results. The reported rendering metrics for our comparison with related work are computed on the *keyframe* images based on the estimated poses, as is standard. However, this can give a warped view on the quality of a method. We want to highlight several key points:

- Every method has a *different keyframe management* or builds their graph based on different thresholds.
- *Not all metrics are reportedly available on all datasets.* We omitted an extensive evaluation of related work due to time constraints. Example: $L1$ metric is only readily available for Replica [37], however due to being a virtual dataset this metric is already quite saturated. The TUM-RGBD [38] benchmark is much more interesting.
- *Performance should be measured both on training and other frames!* Generalization of our test-time optimization is what normally counts, which is why we report results

on non-training frames.

- The *difference between modes* only becomes apparent when considering both geometry and predicted images for both training and other frames.

We show our full evaluation metrics of the overall best results in Table 8. We can only see a clean progression from monocular to *RGBD* inputs on the challenging TUM-RGBD [38] benchmark. We want to highlight, that strict monocular methods can overfit the appearance of training frames very well independent of tracking accuracy or geometric accuracy. However, we can generalize better and achieve much more accurate geometry when using additional depth priors. The benefit of a monocular prior [51] seems to be much smaller on Replica [37]. We found out in Table 9, that depending on the depth supervision signal this result changes. We also suspect concurrent work [33] to supervise with a filtered depth map for this reason. Figure 6 and 7 show qualitative examples on top to get a feeling for how good methods work. We specifically chose non-training frames, which might put us at a disadvantage. We can observe clear improvements on fine-structured details, such as the lamp or background.

Due to our dense map both in tracking and rendering we

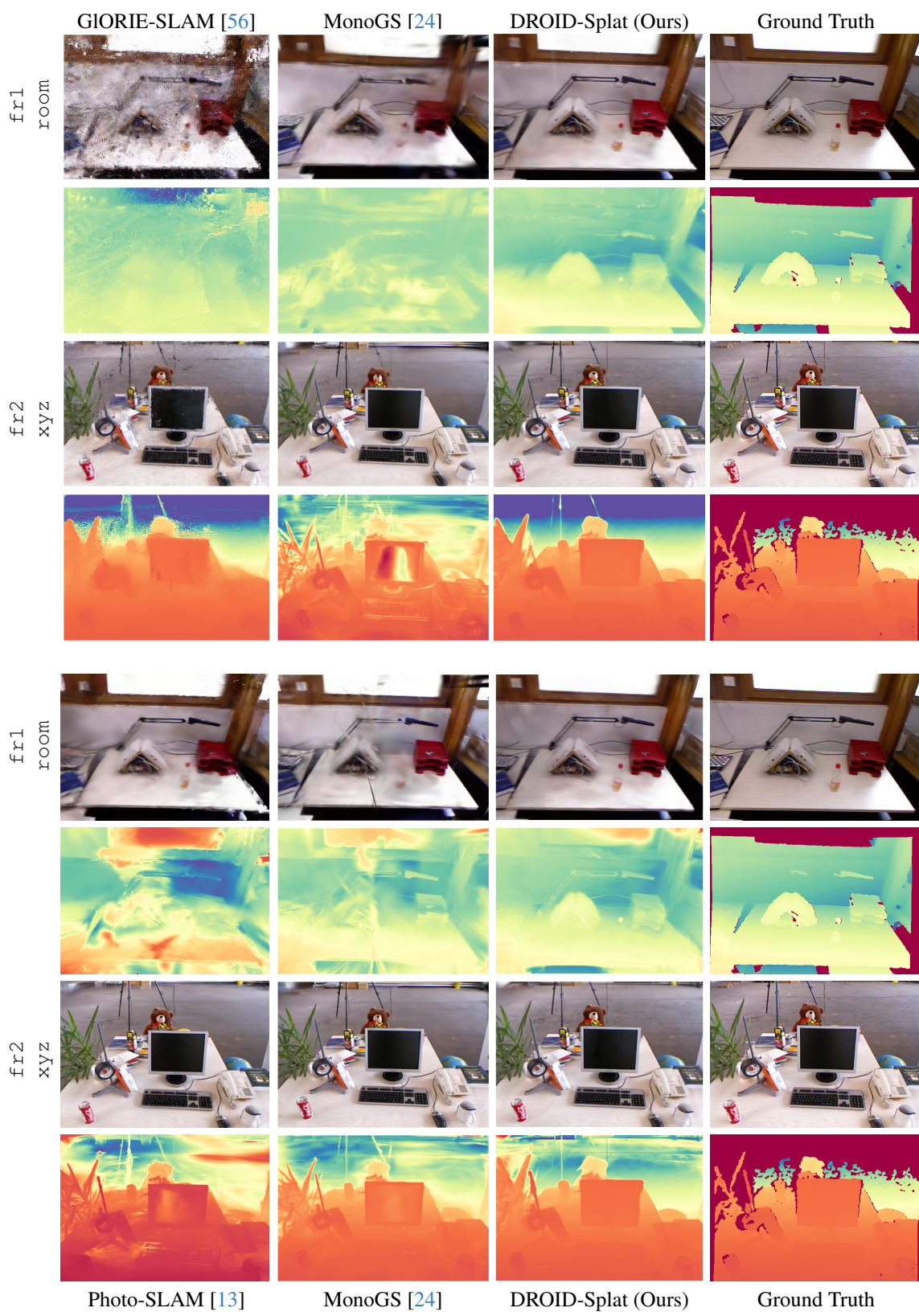


Figure 6. More Rendering Results on TUM-RGBD [38]. Top four rows are from *monocular* input, bottom from *RGBD*.

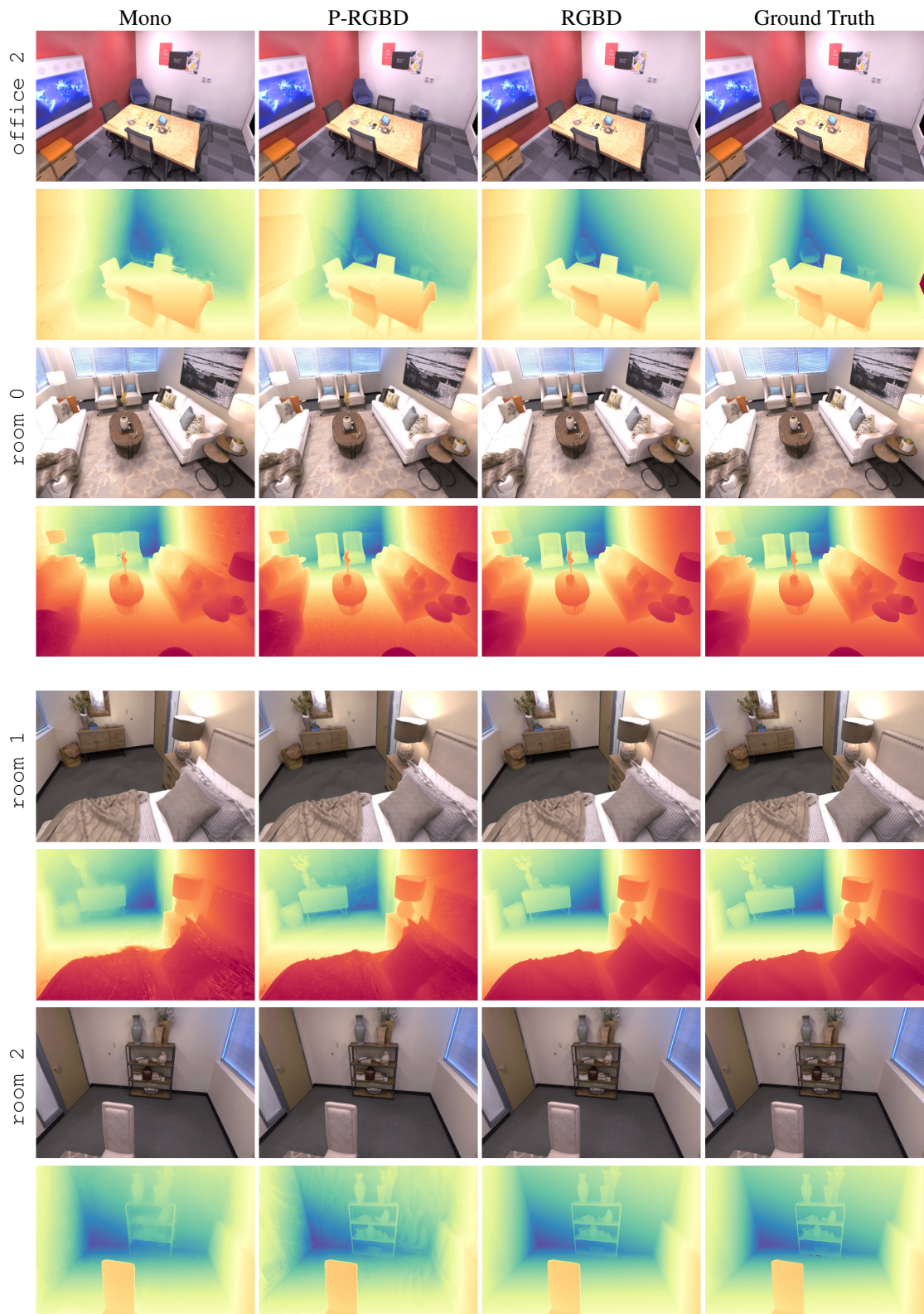


Figure 7. **Rendering Results on Replica [37].** We show non-training frames in multiple input modalities. Note how visually close the predictions are to the groundtruth.

Technique	# Gaussians	PSNR \uparrow	KF		Non-KF		
			LPIPS \downarrow	L1 \downarrow	PSNR \uparrow	LPIPS \downarrow	L1 \downarrow
<i>no refinement</i>							
2DGS [12]	173 309	20.71	0.31	10.2	19.84	0.33	10.3
3DGS [18]	111 878	23.26	0.23	9.1	22.46	0.25	9.2
+ MCMC [19]	113 060	23.78	0.21	8.2	22.81	0.23	8.4
<i>with refinement</i>							
2DGS [12]	131 576	22.87	0.21	8.8	21.73	0.23	8.7
3DGS [18]	88 280	25.98	0.14	8.2	24.47	0.16	8.2
+ MCMC [19]	119 100	26.53	0.13	8.5	24.81	0.15	8.4

Table 10. **Ablation Rendering Techniques.** We report results averaged over 5 runs on TUM-RGBD [38] in *P-RGBD* mode using [51] as a prior. We show a small progression with and without refinement. While 2D Gaussian Splatting [12] quickly produces smooth surfaces, this is not rewarded in the $L1$ error metric.

can achieve better reconstructions than related work. For monocular reconstructions, we specifically show our results with a depth prior [51], which achieves much more accurate geometric reconstruction and better photo-realism on non-training frames than the monocular counter-part. This holds true even for slightly worse $L1$ metrics on Replica, as can be seen in the qualitative images. Results on Replica are

already so accurate, that slight scale differences across time can create slightly non-flat walls. Table 10 shows a detailed ablation of Rendering techniques. We did not combine 2D Gaussian Splatting with the improved densification strategy [19], however we expect this to gain a similar improvement. We did not succeed in achieving better reconstructions for 2D Gaussian Splatting on TUM-RGBD [38]. However, we



Figure 8. **Geometry vs. appearance.** We found, that 2D Gaussian Splatting [12] can quickly create smooth surfaces and does not accumulate many floaters in outdoor scenes. However, the rendering quality lacks behind 3D Gaussian Splatting [18] and as long as good supervision exists we can achieve better $L1$ metrics with 3D Gaussian Splatting.

observe a clear benefit of this representation similar to the results in the respective paper, see examples in Figure 8. We can quickly converge to flat surfaces, which helps to avoid many floaters in outdoor-scenarios. On the used indoor datasets, vanilla 3D Gaussians perform better.

3. Monocular Depth Prediction

Monocular depth prediction is a longstanding task with very impressive in-the-wild results of recent SotA models [2, 11, 49, 51]. We show some qualitative comparisons between selected models in Figure 9. Due to training on massive

datasets, current single-image depth predictions can recover fine-structured details. Nonetheless, the accuracy of rel. depth on a single frame is not the only thing that matters for SLAM. We want to highlight:

- *The rel. depth error on a single image should be minimal.* This is obvious, however most recent models are only evaluated on specific benchmarks such as e.g. KITTI [9] or NYU [36]. Even though model predictions can look qualitatively very different, their abs. rel. error does not seem to be that different on untypical depth prediction benchmarks.
- *Temporal consistency matters a lot.* Even though we op-

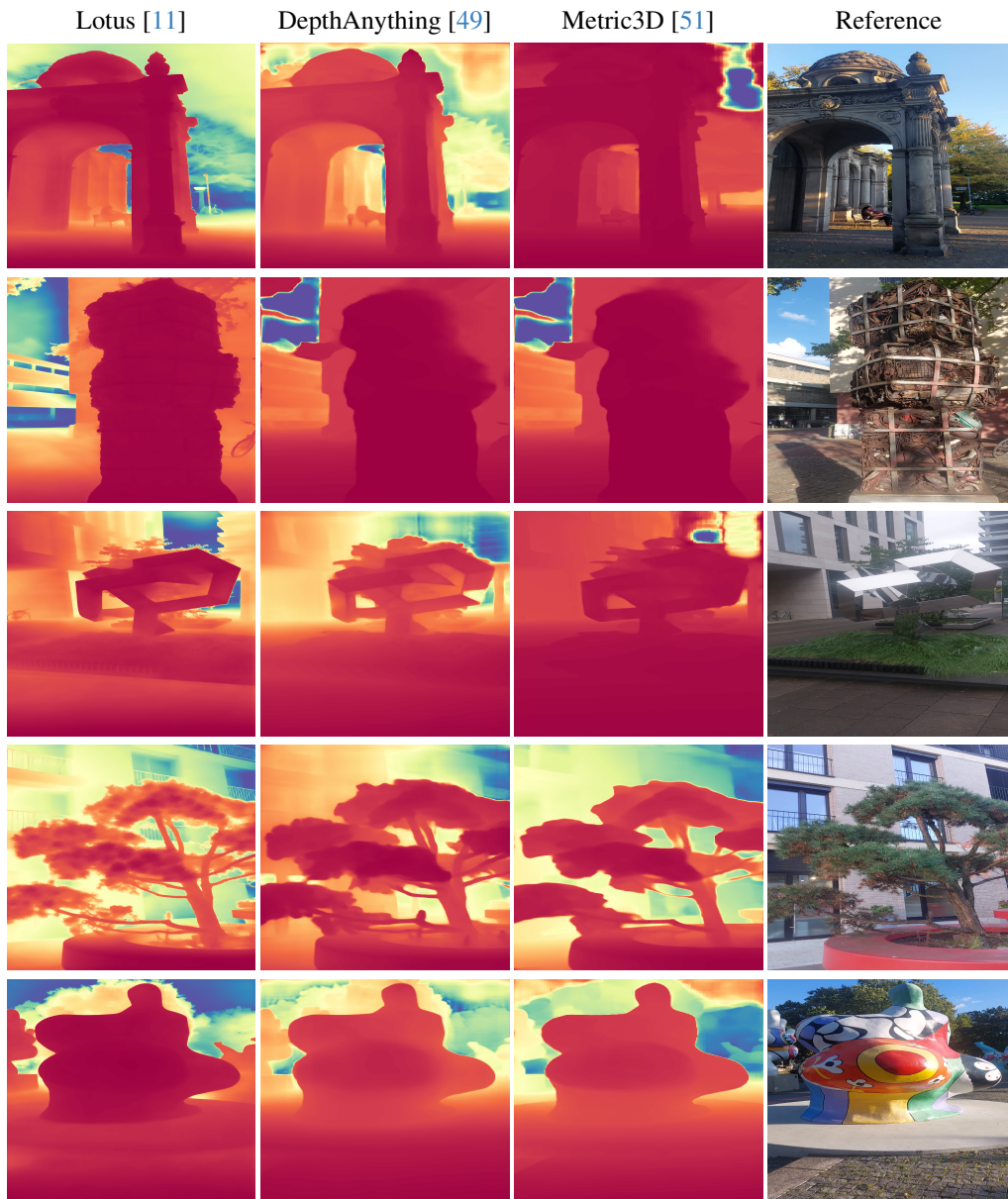


Figure 9. **Monocular depth prediction in-the-wild.** Models exhibit very clear differences w.r.t captured details and scale consistency on self-captured video. Problems can arise in particular for reflective surfaces or paintings.

Prior	ATE RMSE↓	PSNR↑	LPIPS↓	L1↓	ATE RMSE↓	PSNR↑	LPIPS↓	L1↓
	<i>KF</i>				<i>Non-KF</i>			
<i>TUM-RGBD</i>								
Metric3D [51]	1.93	23.27	0.226	0.091	1.83	22.48	0.242	0.089
ZoeDepth [2]	1.97	23.21	0.233	0.132	1.87	22.34	0.249	0.136
DepthAnything [49]	1.91	23.24	0.229	0.098	1.79	22.43	0.246	0.099
Lotus [11]	2.45	22.84	0.256	0.297	2.39	21.84	0.273	0.313
<i>Replica</i>								
Metric3D [51]	0.269	32.92	0.134	0.037	0.268	32.62	0.134	0.038
ZoeDepth [2]	0.266	33.24	0.123	0.088	0.265	32.89	0.123	0.091
DepthAnything [49]	0.268	33.06	0.131	0.063	0.268	32.73	0.131	0.066
Lotus [11]	0.275	32.23	0.116	0.295	0.278	31.72	0.118	0.318

Table 11. **Ablation Prior Depth on Replica [37] and TUM-RGBD [38]**. Recent SotA depth prediction networks [2, 11, 49, 51] have different qualities for SLAM. Good temporal consistency allows accurate geometry reconstruction. However, rendering quality and tracking does not necessarily correlate with it. Results are after online mapping without any refinement using vanilla 3D Gaussian Splatting [18] and averaged over 5 runs.

optimize scale s_i and shift o_i parameters to match our perceived optical flow, models result in differently consistent integrated maps. It is still very beneficial to have high temporal scale consistency in a depth model.

Recent diffusion models [11, 15] can leverage *billion-scale* text-to-image pretraining to achieve strong depth prediction results with little finetuning. As can be seen in Figure 9, the qualitative difference and recovered fine-structured details compared to models trained only on *million-scale* depth prediction datasets seems obvious. However, diffusion models exhibit strong scale differences across a video. This seems to create a lot of floaters, in part enhanced due to the high-frequency details. We did not see an improvement for SLAM by integrating these models for this reason. Table 11 shows the performance of our system with vanilla 3D Gaussian Splatting [18]. We observe that *Metric3D* [51] consistently optimizes the best geometry. However, other metrics are not always consistent.

4. How important is camera calibration really?

In this section we want to show some qualitative examples of in-the-wild footage with unknown intrinsics. As stated in the main paper, we perform a two-stage reconstruction:

1. Run the system without scale-optimization and optimize the camera intrinsics θ .
2. Use the now calibrated camera to run in *P-RGBD* mode and additionally optimize s_i and o_i

Since we need an initial estimate of the intrinsics, we assume a heuristic where for a pinhole camera

$$\begin{aligned} fx = fy &= (H + W) / 2 \\ cx = W/2 \quad cy &= H/2 \end{aligned} \quad (9)$$

The benefit of camera calibration was quantitatively shown

in [10]. We report qualitative results on self-recorded scenes and show the robustness when initializing from a heuristic. It can be seen in Figure 10, that both intrinsics calibration and scale optimization are beneficial for in-the-wild reconstruction. With wrong intrinsics, we observe distorted odometry and structure. With scale optimization, we can generate globally consistent maps. All together forms a good basis for rendering.

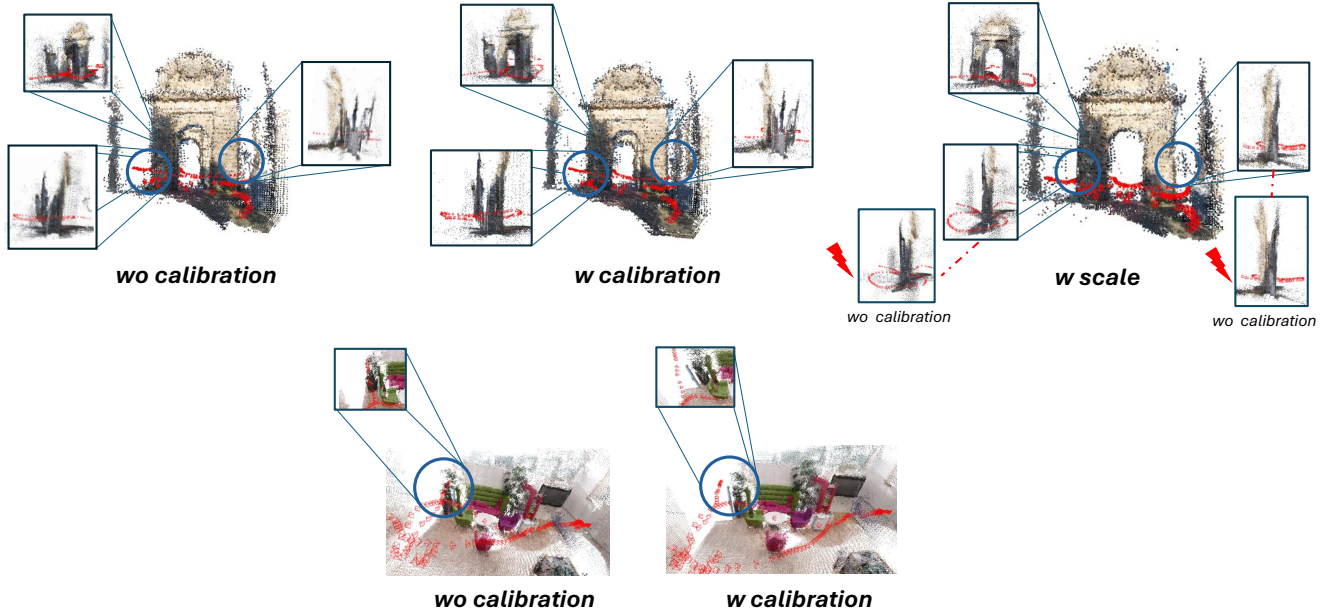


Figure 10. **Camera calibration and prior integration matter.** Distortion effects and artifacts both on the map and camera odometry can be observed without calibration. Using our strategy, we can get rid of distortions. The scale-optimized prior integration allows accurate structure reconstruction. Outdoor scenes require all together due to scale inconsistencies of common depth prediction models.

5. Failure Cases

Due to the challenging unbounded outdoor setting on uncalibrated cameras, we quickly observed common limitations of our framework. We notice that even though monocular depth prediction networks allow highly detailed single-frame predictions, their usage on in-the-wild video is limited. Scale inconsistencies and inaccurate predictions make us accumulate floaters over time. We therefore have to use the following: We limit depth supervision to consistent 3D points using the covisibility check [41] and pixels with confidence $\sigma_i \geq 0.1$. This removes the sky and many floaters, but can also underconstrain the scene.

6. What did not work?

We tried the following things unsuccessfully:

- Multi-View Gaussian Splatting [5] backprojects crops of 2D appearance error into 3D by using the camera ray. We can then perform an intersection test to carve out a 3D volume across multiple views. This test identified new Gaussians, that cause a high 2D error, but were not identified in the original densification strategy [18]. However, we did not manage to improve densification this way within our framework.
- [39] uses a regularization term to battle catastrophic forgetting. We did not succeed on improving our metrics this way. We further tried to simply scale the gradients of optimized Gaussians by the number of times its frame has been already optimized by the renderer.

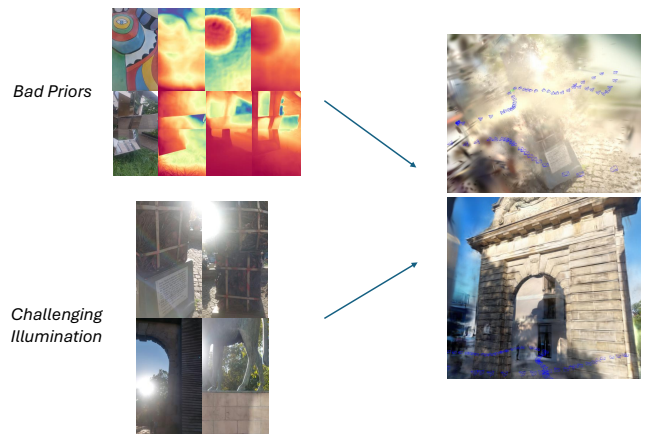


Figure 11. **Common failure cases.** Since we are heavily dependent on depth priors on in-the-wild video, our method can fail when priors get unreliable. Similarly, if the geometry supervision is not good enough, we accumulate floaters on outdoor scenes. Challenging lighting conditions can enhance this effect, since our model will overfit the scene and create additional Gaussians for modeling lighting effects (see Gaussians surrounding object).

- Sparse GS [47] uses a *softmax* for rendering depths. We can identify floaters on outdoor scenes by analyzing the modality of the depth distribution. Since we compute an integrated absolute depth and supervise with priors, we were not able to converge quickly to the correct values due to the used *logarithm* function. Since Sparse GS was created with rel. depth supervision, we did not pursue this further.